Received: Added at production | Revised: Added at production | Accepted: Added at production

DOI: xxx/xxxx

RESEARCH ARTICLE

On the performance of WENO/TENO schemes to resolve turbulence in DNS/LES of high-speed compressible flows

Arash Hamzehloo*[1] | David J. Lusher[2] | Sylvain Laizet[1] | Neil D. Sandham[2]

[1]Turbulence Simulation Group, Department of Aeronautics, Imperial College London, Exhibition Road, London, SW7 2AZ, United Kingdom

[2]Aerodynamics and Flight Mechanics Group, University of Southampton, Boldrewood Innovation Campus, Burgess Road, Southampton, SO16 7QF, United Kingdom

Correspondence
*Arash Hamzehloo, Department of Aeronautics, Imperial College London.
Email: a.hamzehloo@imperial.ac.uk

Abstract

High-speed compressible turbulent flows typically contain discontinuities and have been widely modelled using Weighted Essentially Non-Oscillatory (WENO) schemes due to their high-order accuracy and sharp shock capturing capability. However, such schemes may damp the small scales of turbulence, and result in inaccurate solutions in the context of turbulence-resolving simulations. In this connection, the recently-developed Targeted Essentially Non-Oscillatory (TENO) schemes, including adaptive variants, may offer significant improvements. The present study aims to quantify the potential of these new schemes for a fully-turbulent supersonic flow. Specifically, DNS of a compressible turbulent channel flow with $M = 1.5$ and $Re_\tau = 222$ is conducted using OpenSBLI, a high-order finite difference CFD framework. This flow configuration is chosen to decouple the effect of flow discontinuities and turbulence and focus on the capability of the aforementioned high-order schemes to resolve turbulent structures. The effect of the spatial resolution in different directions and coarse grid implicit LES are also evaluated against the WALE LES model. The TENO schemes are found to exhibit significant performance improvements over the WENO schemes in terms of the accuracy of the statistics and the resolution of the three-dimensional vortical structures. The 6^{th} order adaptive TENO scheme is found to produce comparable results to those obtained with non-dissipative 4^{th} and 6^{th} order central schemes and reference data obtained with spectral methods. Although the most computationally expensive scheme, it is shown that this adaptive scheme can produce satisfactory results if used as an implicit LES model.

KEYWORDS:
TENO; High-order; Channel flow; OpenSBLI; Code generation; GPU

1 | INTRODUCTION

High-speed compressible turbulent flows play a significant role in a variety of advanced fluid mechanics related applications and disciplines such as supersonic or hypersonic aerodynamics and combustion, aerospace propulsion, inertial confinement fusion and astrophysics[1,2,3,4,5]. Those flows typically contain shockwaves and flow discontinuities, and have been widely modelled using Weighted Essentially Non-Oscillatory (WENO) schemes[6,7] due to their high-order accuracy and sharp shock/discontinuity capturing capability. However, those schemes, which aim to stabilise the solution by adding numerical dissipation, may damp some scales of turbulence and as a consequence result in inaccurate solutions in the context of turbulence-resolving simulations,

unless excessively fine spatial resolutions are used which is not practical for Direct Numerical Simulation (DNS) of complex flows[8]. Therefore, it is of great importance to critically evaluate and quantify the ability of such high-order schemes to accurately predict the wide range of flow structures in compressible turbulent flows.

There are not many studies available in the literature discussing and comparing the performance of modern high-order shock capturing schemes to resolve compressible turbulence, particularly in wall-bounded flows. Mossi and Sagaut[9] were among the first to investigate the performance of high-order shock capturing schemes for compressible turbulent flows. Specifically, they performed direct and Large Eddy Simulations (LES) on quasi-incompressible ($M = 0.5$) and compressible ($M = 1.5$) turbulent channel flows (TCFs) using 2^{nd} order central and 3^{rd} order Total Variation Diminishing (TVD) Roe schemes. They reported that the TVD scheme performed poorly in capturing turbulent structures mainly due to its significant numerical diffusion. Gerolymos et al.[10] used high-order upwind, WENO and mapped WENO[11] schemes to conduct DNS of subsonic ($M = 0.35$) and supersonic ($M = 1.5$) turbulent channel flows. It was noticed that very high-order upwind schemes could reproduce results obtained by pseudospectral schemes, given slightly higher spatial resolutions. However, noticeable numerical diffusion was reported for the WENO schemes. Gerolymos et al.[10] also provided a brief review of some early DNS studies on TCFs using high-order methods.

The performance of the WENO scheme can be improved by using a dynamic balance between an upwind formulation for high gradient and shock-containing regions and a central formulation in smooth regions such as the method proposed in a bandwidth-optimised WENO scheme, namely WENO-SOL[12]. Taieb and Ribert[13] used the WENO-SOL scheme to perform DNS and LES of supersonic channel flows ($M = 1.5$). The 5^{th} order scheme performed well in the context of DNS. It was also used without and with Sub-Grid Scale (SGS) models to perform LES of TCFs. Without an SGS model, the WENO-SOL scheme was used as an Implicit LES (ILES) model and exhibited a satisfactory performance. The performance of the WENO-SOL scheme was improved when it was combined with a dynamic SGS LES model and produced a very close behaviour to DNS. The worst performance of the WENO-SOL scheme was for when it was combined with a non-dynamic SGS LES model mainly due to issues related to overdissipation[13]. Ribert et al.[14] extended the WENO-SOL scheme and also the WENO scheme developed by Jiang and Shu (WENO-JS)[6] for real fluids in order to perform LES of turbulent channel flows under supercitical conditions. Under such conditions, where tiny variations in main flow parameters could significantly alter the fluid properties and impose considerable gradients, applying a shock capturing scheme could greatly improve the stability of the solution. A comparison of some 5^{th} and 6^{th} order shock capturing schemes of the WENO family to model low Mach ($M = 0.01, 0.1$ and 0.3) TCFs has also been reported by Matsuyama[15]. Various schemes including WENO-JS, WENO-Z[16], Linear WENO (LWENO)[17] and WENO with a relative limiter (WENO-RL)[18] were investigated[15]. Again, the dissipative behaviour of the WENO scheme was highlighted and the use of its modified versions, such as the WENO-RL scheme, which could noticeably reduce the dissipation, was emphasised.

In addition to channel flows, the performance of various high-order shock capturing schemes, mainly from the WENO family, to resolve compressible turbulent flows have been investigated in the context of turbulent boundary layers, isotropic decaying turbulence and Shock-Boundary Layer Interactions (SBLIs). Similarly to the aforementioned TCF cases, different modifications were also applied to overcome the destructive dissipative behaviour of the WENO scheme. Lagha et al.[19] successfully performed DNS of turbulent boundary layers with Mach number values up to $M = 20$ using a 5^{th} order WENO scheme. Specifically, the authors used the WENO scheme at high gradient regions and a 5^{th} order upwind scheme for smooth regions with global Lax-Friedrichs flux splitting. Supersonic turbulent boundary layers were also studied by Duan et al.[20] using a 7^{th} order WENO scheme with limiters to reduce the numerical dissipation. Johnsen et al.[21] studied the performance of various high resolution shock capturing schemes on a variety of problems including the Taylor-Green Vortex (TGV) and shock-dominated problems such as the Shu-Osher problem, a shock-vorticity interaction and the Noh problem all on under-resolved grids. The authors applied and compared several methods including WENO, hybrid WENO/central, artificial diffusivity, an adaptive characteristic-based filter and a shock fitting method. It was concluded that the WENO and the artificial diffusivity method (which used the magnitude of the strain-rate to activate the artificial viscosity) were not suitable for high-fidelity modelling of compressible turbulence. However, modified artificial diffusivity methods which use dilatation to activate the artificial viscosity were found to be able to resolve compressible turbulence. The hybrid WENO/central method was effective in reducing the numerical dissipation but quite challenging with respect to developing effective shock sensors[21].

Brehm et al.[22] also compared the performance of various high-order shock capturing schemes on a variety of problems including the Shu-Osher problem, the isentropic vortex convection problem, double Mach reflection and a TGV problem. The authors used central finite difference schemes with explicit artificial dissipation, a compact central finite difference scheme with localised artificial diffusivity and various modified WENO schemes (a 6^{th} order WENO by Hu et al.[23], a 5^{th} order WENO by Ghosh and Baeder[24] and WENO-Z) in both explicit and compact finite difference forms and on different grid resolutions. Based

on their decaying isotropic turbulence case, the authors reported that the 5^{th} order compact WENO and the 6^{th} order WENO resolved the small scale flow structures better compared to a 5^{th} order WENO-Z. It was also noted that the highest spectral resolution was obtained by the localised scheme followed by the 5^{th} order compact WENO and the the 6^{th} order WENO[22]. Karami et al.[25] used a hybrid 5^{th} order WENO/6^{th} order central scheme to perform LES of various flow configurations including a compressible round jet and an underexpanded impinging jet. The authors proposed a new shock sensor based on a WENO smoothness indicator. A comprehensive study on the performance of various shock sensors for hybrid WENO-based schemes was recently conducted by Zhao et al.[26]. The authors also proposed a new shock sensor for WENO-based hybrid schemes which was not affected by the numerical dissipation caused by the WENO scheme. Hoffmann et al.[27] used a hybrid Summation-By-Parts (SBP) central scheme and a 5^{th} order WENO scheme to perform LES of transitional flow over a flat plate with an impinging shock and also turbulent flow over a compression corner. The blending approach of the abovementioned upwind/central-WENO hybrid schemes requires a great care to ensure numerical conservation and stability at the interface of different schemes used. Non-linear filter schemes[28,29,30,31] are developed to avoid this interface deficiency of high-order hybrid schemes. Specifically, a hybrid scheme is applied to the inviscid fluxes and the non-linear fluxes are typically evaluated by central discretisation of an entropy conservative formulation.

In a prework to the present contribution, Lusher and Sandham[8] conducted a study of the performance of various high-order shock capturing schemes to model a compressible TGV and a transitional supersonic SBLI. The authors used 4^{th} order central, 5^{th} and 7^{th} order WENO-Z, 5^{th} order WENO-JS and also various orders and formulations of the Targeted Essentially non-Oscillatory (TENO) family scheme[32,33,34,35]. A significant improvement was obtained with the TENO schemes over the WENO schemes.

It is evident that there are limited works available in the literature that provide direct comparisons of the performance of various high-order shock capturing schemes to accurately resolve turbulence in compressible high-speed wall-bounded flows. Also, the majority of the earlier works are based on schemes from the WENO family which have shown significant dissipative behaviours and failed to accurately resolve turbulent structures. The present work aims to compare and quantify the performance of the existing high-order shock capturing schemes, including the TENO family schemes, to model fully-turbulent supersonic flows. The focus is on the capability of those schemes to resolve turbulent structures and predict statistical quantities. Therefore, a channel flow configuration is used to decouple the effect of flow discontinuities and turbulence. Specifically, it extends the earlier work of Lusher and Sandham[8] to supersonic TCFs. Additionally, the present study evaluates the performance of such high-order schemes in the context of ILES by making direct comparisons against DNS and explicit LES approaches.

2 | COMPUTATIONAL METHODOLOGY

2.1 | Governing equations

The dimensionless governing equations of a compressible Newtonian fluid flow that conserve mass, momentum and energy are given as:

$$\frac{\partial \rho}{\partial t} + \frac{\partial}{\partial x_j}(\rho u_j) = 0, \tag{1}$$

$$\frac{\partial \rho u_i}{\partial t} + \frac{\partial}{\partial x_j}(\rho u_i u_j + p\delta_{ij} - \tau_{ij}) + c_j \delta_{ij} = 0, \tag{2}$$

$$\frac{\partial \rho E}{\partial t} + \frac{\partial}{\partial x_j}(\rho E u_j + u_j p + q_j - u_i \tau_{ij}) + c_j u_j = 0, \tag{3}$$

where ρ represents the density, $u_i (i = 0, 1, 2)$ denotes the velocity component in the i^{th} direction, E is the total energy, and p and δ denote the pressure and the Kronecker delta, respectively. The equations are solved in three spatial dimensions $x_i (i = 0, 1, 2)$. c_i is a constant forcing term, which drives the flow, with a value of unity in the x_0 direction and zero in other directions. Moreover, τ_{ij} and q_j are the viscous stress tensor and the heat flux (based on Fourier's law) respectively, defined as:

$$\tau_{ij} = \frac{\mu}{Re^*_\tau}\left(\frac{\partial u_i}{\partial x_j} + \frac{\partial u_j}{\partial x_i} - \frac{2}{3}\frac{\partial u_k}{\partial x_k}\delta_{ij}\right), \tag{4}$$

$$q_j = \frac{-\mu}{(\gamma - 1)M^{*2}_\tau Pr Re^*_\tau}\frac{\partial T}{\partial x_j}, \tag{5}$$

where μ denotes the dynamic viscosity, T is the temperature, Pr is the Prandtl number. Also, Re^*_τ and M^*_τ denote the Reynolds and Mach numbers based on a friction velocity defined as $u^*_\tau = \sqrt{\langle \tau_{wall} \rangle / \langle \rho \rangle}$ where τ_{wall} denotes the wall shear stress and $\langle \rho \rangle$ is the bulk-averaged density. Angle brackets $\langle \rangle$ denote averages over the homogeneous spatial directions and time throughout this paper. The dynamic viscosity, if required, is calculated as $\mu = T^{0.7}$. Also, since the governing equations are solved for the conserved variables (ρu_i and ρE), then the velocity field is obtained by $u_i = \frac{\rho u_i}{\rho}$ and the temperature is calculated as $T = \frac{p \gamma M^{*2}_\tau}{\rho}$. Here the pressure of an ideal Newtonian fluid is obtained using an equation of state as:

$$p = (\gamma - 1)(\rho E - \frac{1}{2}\rho u_i u_i). \tag{6}$$

All quantities are non-dimensionalised by the bulk-averaged density, the friction velocity (u^*_τ) and the wall temperature. It is worth mentioning that the governing equations with the WENO and the TENO schemes are solved as presented in equations 1–3 and when central schemes are used a skew-symmetric formulation is applied to the convective terms[36].

2.2 | Flux reconstruction and shock capturing schemes

In the present work the governing equations are discretised by applying finite differencing within OpenSBLI, a high-order Computational Fluid Dynamics (CFD) framework[37]. Comprehensive discussions on the WENO and TENO schemes implemented in OpenSBLI can be found in[8,38]. However, a brief discussion on the flux reconstruction and the aforementioned shock capturing methods in OpenSBLI is provided here for completeness.

To discretise the governing equations, their fluxes need to be reconstructed at each discrete grid point. With the finite difference approach, the flux reconstruction can be performed in each direction independently. For example, a $1D$ hyperbolic equation of the form $U_t + f(U)_x = 0$ can be discretised by reconstructing the flux term $f(U)_x$ over mid-point (half-node) locations with grid spacing Δx as follows:

$$\frac{\partial U}{\partial t} + \frac{1}{\Delta x}(\hat{f}_{i+\frac{1}{2}} - \hat{f}_{i-\frac{1}{2}}) = 0, \tag{7}$$

where $i-\frac{1}{2}$ and $i+\frac{1}{2}$ denote mid-point locations between grid point i and grid points $i-1$ and $i+1$ in the x direction, respectively. The full numerical stencil is reconstructed from a convex combination of lower order stencils as shown for WENO in[38] and TENO in[8]. Mid-point fluxes in equation 7 are calculated as a weighted sum of Essentially Non-Oscillatory (ENO) interpolations over a set of r candidate stencils as:

$$\hat{f}_{i\pm\frac{1}{2}} = \sum_{r=0}^{K-1} \omega_r \hat{f}^{(r)}_{i\pm\frac{1}{2}}, \tag{8}$$

where $\hat{f}^{(r)}_{i\pm\frac{1}{2}}$ are evaluated using the classical ENO scheme of Shu[7] and ω_r are the non-linear weights. The order of the WENO scheme is equal to $2K-1$ and for instance $K=3$ for a 5^{th} order scheme which results in $r = 0, 1, 2$ candidate stencils[38].

One difference between WENO and TENO schemes stems from the way that the non-linear weights of equation 8 are calculated. In WENO schemes ω_r is defined as:

$$\omega_r = \frac{\alpha_r}{\sum_{s=0}^{k-1} \alpha_s}, \quad r = 0, ..., k-1, \tag{9}$$

where α_r for the WENO-JS and the WENO-Z schemes are defined as $\alpha_r = \frac{d_r}{(\epsilon+\beta_r)^2}$ and $\alpha_r = d_r(1 + \frac{\tau_k}{\beta_r+\epsilon})$, respectively. The polynomial smoothness indicator β_r ensures that stencils containing shocks are weighted close to zero. The optimal linear weights for the smooth (shock-free) regions is denoted by d_r. Also, τ_k is a global smoothness indicator over the full numerical stencil. It should be noted that ϵ is typically considered to be 1×10^{-6} to avoid division by zero[8].

The TENO scheme also introduces a discrete cut-off function that removes non-smooth candidate stencils from the flux reconstruction. Smooth candidate stencils are included in the reconstruction with their ideal linear weight to reduce the numerical dissipation compared to the WENO scheme[8]. For the TENO schemes ω_r is defined as:

$$\omega_r = \frac{d_r \delta_r}{\sum_{s=0}^{K-3} d_r \delta_r}, \quad \delta_r = \begin{cases} 0 \text{ if } \chi < C_T \\ 1 \text{ otherwise} \end{cases} \tag{10}$$

where C_T is a adjustable cut-off parameter and χ denotes the smoothness measure defined as $\chi = \frac{\gamma_r}{\sum_{r=0}^{K-3} \gamma_r}$ with $\gamma_r = (C + \frac{\tau_K}{\beta_r+\epsilon})^q$ and $r = 0, ..., K-3$[8]. The parameters C and q control the levels of dissipation invoked by the non-linear weights and

typically have values of 1 and 6, respectively[32,8]. It is worth mentioning that reducing the value of C_T reduces the numerical dissipation (which is desirable for compressible turbulence) at the cost of increased spurious oscillations in the vicinity of flow discontinuities. Values of 1×10^{-5} and 1×10^{-7} are suggested for the 5^{th} order and 6^{th} order TENO, respectively[8,32].

A shock sensor (Φ) can be added to the TENO scheme to adjust the threshold of the C_T parameter in different regions of the domain and discard fewer stencils from the reconstruction in smooth regions [8,34,35]. In this work, a modified version of the Ducros sensor[39] is used to develop an adaptive TENO scheme (TENO-A) as discussed in[8]. This sensor, which was designed to distinguish between dilatation rate (at shocks) and vorticity (in turbulence), was found to be more robust in the OpenSBLI framework[8]. Nevertheless, the sensor type would not have a noticeable effect on the results of the present study due to the absence of shocks and flow discontinuities. C_T is dynamically adjusted by the shock sensor Φ as $C_T = 10^{-\left\lfloor \alpha_1 - \alpha_2(1-g(\Phi)) \right\rfloor}$, where $g(\Phi) = (1-\Phi)^4(1+4\Phi)$ and $\lfloor\rfloor$ is the Gauss bracket[35,8]. The adjustable parameters α_1 and α_2 are taken as $\alpha_1 = 10.5$ and $\alpha_2 = 4.5$ in the present study.

The viscous terms in equations 1–3 are computed with a 4^{th} order central scheme for the internal domain and over periodic boundaries, for non-periodic boundaries a 4^{th} order one-sided boundary closure is used[8,40]. The solution is advanced in time using a low-storage 3 stage explicit Runge-Kutta scheme[41].

2.3 | WALE LES model

In the present study the performance of an explicit LES model, specifically the Wall-Adapting Local Eddy-viscosity (WALE) SGS model, is evaluated against those of DNS as well as ILES approaches. The original WALE formulation developed by Nicoud and Ducros[42] is implemented in OpenSBLI. The WALE model considers the effects of the strain and rotation rates of the resolved flow field. Specifically, in this model the turbulent (eddy) viscosity is evaluated as:

$$\mu_t = \rho(C_w\Delta)^2 \frac{(S^d_{ij}S^d_{ij})^{3/2}}{(\overline{S}_{ij}\overline{S}_{ij})^{5/2} + (S^d_{ij}S^d_{ij})^{5/4}}, \tag{11}$$

where $\overline{S}_{ij}$ is the deformation tensor of the resolved flow field defined as $\overline{S}_{ij} = \frac{1}{2}\left(\frac{\partial \overline{u}_i}{\partial x_j} + \frac{\partial \overline{u}_j}{\partial x_i}\right)$. Also, S^d_{ij} is the traceless symmetric part of the square velocity gradient defined as $S^d_{ij} = \frac{1}{2}\left(\overline{g}^2_{ij} + \overline{g}^2_{ji}\right) - \frac{1}{3}\delta_{ij}\overline{g}^2_{kk}$ with $\overline{g}^2_{kk} = \overline{g}_{ik}\overline{g}_{kj}$ where $\overline{g}_{ij}$ is the velocity gradient tensor defined as $\overline{g}_{ij} = \frac{\overline{u}_i}{\partial x_j}$. Moreover, Δ is the subgrid characteristic length scale, which in this study is defined as $\Delta = V^{1/3}$ where V is proportional to the local grid spacing as $V = \Delta x \Delta y \Delta z$. C_w is the SGS model constant which has a value of $C_w = 0.325$ in the present study. It should be noted that overbar here denotes the resolved flow quantities.

To conduct LES simulations using the WALE model in OpenSBLI, the same governing equations as presented in equations 1 – 3 are solved for the resolved flow field. However, the effect of the turbulent viscosity is added to the viscous stress tensor and the heat flux (equations 4 and 5) as $\tau_{ij} = (\frac{\mu}{Re^*_\tau} + \mu_t)(\frac{\partial \overline{u}_i}{\partial x_j} + \frac{\partial \overline{u}_j}{\partial x_i} - \frac{2}{3}\frac{\partial \overline{u}_k}{\partial x_k}\delta_{ij})$ and $q_j = (\frac{-\mu}{(\gamma-1)M^{*2}_\tau PrRe^*_\tau} - \frac{\mu_t}{(\gamma-1)M^{*2}_\tau Pr_t})\frac{\partial \overline{T}}{\partial x_j}$. The turbulent Prandtl number has a value of $Pr_t = 1.0$ in the present study. It is worth mentioning that it was found that the results reported here were almost insensitive to the value of Pr_t, at least within the range of values found in the literature for similar studies.

2.4 | OpenSBLI framework

OpenSBLI is a Python-based automatic source code generation and parallel computing framework for finite difference discretisation[37]. It generates C codes for the Oxford Parallel library for Structured mesh solver (OPS), an embedded Domain Specific Language (DSL) with associated libraries and preprocessors to generate parallel executables for applications on multi-block structured meshes[43,44]. OPS can target various computational architectures based on CUDA or OpenCL for GPUs, MPI or OpenMP for CPUs and CUDA-MPI for multiple GPUs[44]. A comprehensive discussion on the automatic derivation Python interface of OpenSBLI and the automatic procedure of the OPS C code generation can be found in[37,38]. The results presented in this paper are obtained using various backends including a single GPU (CUDA), multiple GPUs (MPI+CUDA) and distributed computing with CPUs (MPI).

3 | PROBLEM SPECIFICATIONS

DNS and LES of subsonic and supersonic plane channel flows with a domain size of $4\pi H \times 2H \times \frac{4\pi}{3}H$ are conducted. H denotes the channel half height and is set to $H = 1$ in the present study. The streamwise (x_0), normal (x_1) and spanwise (x_2) directions are denoted as x, y and z as shown in figure 1. Also, u, v and w denote the velocity components in x, y and z directions, respectively. Streamwise and spanwise boundaries are periodic and isothermal no-slip walls are assigned to the boundaries in the normal direction. The grid is stretched in the y direction in order to accurately resolve the near wall region. A hyperbolic tangent stretching function[45] is used as follows:

$$y = 0.5L_y\left\{1.0 - \left[\frac{\tanh\left[f_s\left(1.0 - 2.0\left(\frac{j}{n_y - 1.0}\right)\right)\right]}{\tanh(f_s)}\right]\right\} - 1.0, \tag{12}$$

where L_y denotes the domain length in the y direction (here $L_y = 2$), f_s is the stretching factor and governs the distance ratio between two adjacent grid points, j is the grid point number (starts from 0) and n_y is the total number of grid points in the y direction. In this study a stretching factor of $f_s = 1.7$ is used for TCF simulations unless otherwise stated. It should be noted that the centre of the channel is at $y = 0$ as shown in figure 1.

The test cases studied here are based on an incompressible channel flow with a friction velocity Reynolds number of $Re_\tau = 180$[46] and a compressible channel flow with a friction velocity Reynolds number of $Re_\tau = 222$ and a friction Mach number of $M_\tau = 0.082$[47]. As mentioned earlier the bulk-averaged density $\langle\rho\rangle$ and its corresponding friction velocity ($u^*_\tau = \sqrt{\langle\tau_{wall}\rangle/\langle\rho\rangle}$, where τ_{wall} denotes the wall shear stress defined here as $\langle\tau_{wall}\rangle = \langle\mu^*_{wall}\rangle(\frac{d\langle u_0\rangle}{dx_1})_{x_1=0}$) are used to normalise the governing equations. Therefore, the Reynolds number in equations 4 and 5 is defined as $Re^*_\tau = \frac{\langle\rho\rangle u^*_\tau H}{\langle\mu^*_{wall}\rangle}$ while the friction Reynolds number is defined as $Re_\tau = \frac{\langle\rho_{wall}\rangle u_\tau H}{\langle\mu^*_{wall}\rangle}$ where $u_\tau = \sqrt{\langle\tau_{wall}\rangle/\langle\rho_{wall}\rangle}$. This leads to $Re^*_\tau = Re_\tau\sqrt{\langle\rho\rangle/\langle\rho_{wall}\rangle}$ and $M^*_\tau = M_\tau\sqrt{\langle\rho_{wall}\rangle/\langle\rho\rangle}$. The compressible case has $\frac{\langle\rho_{wall}\rangle}{\langle\rho\rangle} = 1.355$[47] which gives $Re^*_\tau = 190.71$ and $M^*_\tau = 0.0955$ for the governing equations in the present study. For the incompressible case $Re^*_\tau = 180$ and $M^*_\tau = 0.01$ are used. It is clear that for a fully-resolved DNS after collecting sufficiently enough statistical samples one should recover $u^*_\tau = 1.0$.

All simulations are initialised by superimposing a random fluctuation over a mean velocity profile in the streamwise direction and imposing random fluctuations in other directions. Specifically, the initial mean streamwsie velocity ($\overline{u}$) is a piecewise function as:

$$\overline{u} = \begin{cases} (1 - |\ y\ |)\, Re^*_\tau, & (1 - |\ y\ |)Re^*_\tau < 10 \\ \kappa\ln\left((1 - |\ y\ |)\, Re^*_\tau\right) + b \end{cases} \tag{13}$$

where $b = 5.5$, κ is the von Karman constant and has a value of 2.5. Amplitude of the fluctuations is defined as:

$$A = 0.1 \times \left(\kappa\ln(Re^*_\tau) + b\right), \tag{14}$$

and sine and cosine disturbances are applied to the velocity profile in all directions. For the x, y and z directions the sine disturbances are defined as $s_x = \sin\left(\frac{4\pi x}{L_x}\right)$, $s_y = \sin(\pi y)$ and $s_z = \sin\left(\frac{2\pi z}{L_z}\right)$. Similarly, the cosine disturbances are defined as $c_x = \cos\left(\frac{4\pi x}{L_x}\right)$, $c_y = 1 + \cos(\pi y)$ and $c_z = \cos\left(\frac{2\pi z}{L_z}\right)$. L_x, L_y and L_z are the domain dimensions in the x, y and z directions, respectively as shown in figure 1. Finally, the initial values for the velocity components (specified with the subscript 1) are defined as:

$$u_1 = \overline{u} + Ac_x s_y s_z(\frac{L_x}{2}), \tag{15}$$

$$v_1 = -As_x c_y s_z, \tag{16}$$

$$w_1 = -As_x s_y c_z(\frac{L_z}{2}). \tag{17}$$

The initial density is $\rho_1 = 1$ throughout the domain and the initial energy field is imposed as $(\rho E)_i = \frac{p_1}{\gamma - 1} + \frac{1}{2}\rho\left(u_1^2 + v_1^2 + w_1^2\right)$ with the initial pressure field defined as $p_1 = \frac{1}{\gamma M^{*2}_\tau}$.

The incompressible case is solved using the 4^{th} order central scheme on a grid with a $129 \times 129 \times 129$ resolution. The compressible case is solved with the 4^{th} and 6^{th} order central schemes, 5^{th} WENO-JS and WENO-Z schemes, 5^{th} and 6^{th} order TENO scheme, and the 6^{th} order TENO-A scheme. In addition to the grid with $129 \times 129 \times 129$ resolution, the compressible case is also solved on various finer grids as shown in table 1 which summarises the DNS channel flow test cases studied here. Subscript s denotes the actual values obtained from simulations. Based on the earlier discussion in this section one could write $u^*_{\tau_s} = \sqrt{\frac{\langle\rho\rangle}{Re^*_\tau}\frac{d\langle u_0\rangle}{dx_1}}$ and $u_{\tau_s} = \sqrt{\frac{\langle\rho_{wall}\rangle}{Re^*_\tau}\frac{d\langle u_0\rangle}{dx_1}}$ which gives $Re^*_{\tau_s} = \langle\rho\rangle u^*_{\tau_s} Re^*_\tau$ and $Re_{\tau_s} = \langle\rho_{wall}\rangle u_{\tau_s} Re^*_\tau$. Graphs in this work are plotted against the y^+ values obtained in simulations (y^+_s) calculated as $y^+_s = yRe_{\tau_s}$. The normalised cell sizes in different directions, Δx^+_s, Δy^+_s (the height of the first grid point above the wall) and Δz^+_s, are evaluated in a similar way to y^+_s.It is worth mentioning that the reference data for the compressible test case as reported by Coleman et al.[47] are adjusted in this work to reflect the differences in the normalisation approach used. Specifically, the velocity components (and their fluctuating parts) of the reference data are multiplied by a factor of $\frac{\int_{-1}^{1}\langle\rho u_0\rangle dx_1}{\int_{-1}^{1}\langle\rho\rangle dx_1} \approx 16.1$.

Various time steps from $\Delta t = 5\times10^{-5}$ to 2×10^{-4} are used based on the stability of the solution as provided in table 1. Statistics are collected after a fully turbulent flow is established (at $t = 50$) and for a duration of $T = 1000$ (around 1500 flow-through times).

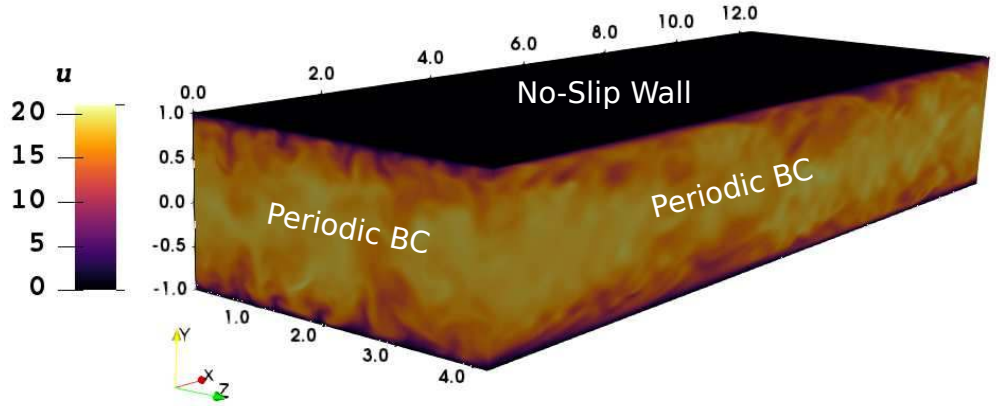

FIGURE 1 Turbulent channel flow geometry, boundary conditions and dimensions. Based on the instantaneous streamwise velocity (u) of the case with $Re_\tau = 180$ at $t = 1050$.

4 | RESULTS AND DISCUSSION

In the following subsections, first the performance of the OpenSBLI computational framework with the central scheme is compared against two incompressible and compressible test cases from the literature[46,47] on a baseline grid resolution ($129 \times 129 \times 129$). Also, a comparison is provided on the performance of various central, WENO and TENO schemes on the baseline grid as shown in table 1. Then the effect of the grid resolution is explored for the central and the TENO schemes as also shown in table 1. Finally, a comparative study is conducted on DNS and LES modelling (explicit and implicit) based on the test cases shown in table 5.

4.1 | Subsonic channel flow

DNS of incompressible turbulent channel flows with friction Reynolds number values around $Re_\tau = 180$ have been reported by several authors since it was first investigated by Kim, Moin and Moser[48]. A review of the earlier simulations of this test case is provided by Vreman and Kuerten[46]. The authors also conducted DNS on a similar channel flow case using two different codes,

TABLE 1 Turbulent channel flow DNS test cases.

Case	Re^*_τ	$Re^*_{\tau_s}$	M_τ	Re_τ	Re_{τ_s}	Scheme (Ord.)	Grid	Δt $\times 10^{-4}$	$\langle u_c \rangle$
1	180	179.836	0.01	180	180.188	Central(4)	129×129 × 129	0.5	18.295
Ref.1	–	–	–	180	180	Spectral	576×577 × 385	–	18.262
2	190.71	189.336	0.082	222	221.814	Central(4)	129×129 × 129	2.0	18.876
2b	190.71	190.036	0.082	222	223.000	Central(4)	257×257 × 257	0.5	18.826
3	190.71	189.333	0.082	222	222.248	Central(4)	257×129 × 129	2.0	18.917
4	190.71	189.997	0.082	222	222.614	Central(4)	129×257 × 129	0.5	18.893
5	190.71	189.365	0.082	222	221.921	Central(4)	129×129 × 257	2.0	18.821
6	190.71	189.367	0.082	222	222.199	Central(6)	129×129 × 129	2.0	18.891
7	190.71	190.136	0.082	222	223.737	TENO(6)	129×129 × 129	2.0	19.045
8	190.71	190.508	0.082	222	223.174	TENO(6)	257×129 × 129	2.0	18.737
9	190.71	190.155	0.082	222	223.805	TENO(6)	129×257 × 129	1.0	19.074
10	190.71	190.524	0.082	222	223.920	TENO(6)	129×129 × 257	2.0	18.903
11	190.71	190.274	0.082	222	226.891	WENO-Z(5)	129×129 × 129	2.0	19.867
12	190.71	188.865	0.082	222	227.144	WENO-JS(5)	129×129 × 129	2.0	20.435
13	190.71	189.561	0.082	222	224.337	TENO(5)	129×129 × 129	2.0	19.382
14	190.71	189.496	0.082	222	223.153	TENO-A(5)	129×129 × 129	2.0	19.058
15	190.71	189.837	0.082	222	222.807	TENO-A(6)	129×129 × 129	2.0	18.897
16	190.71	189.645	0.082	222	222.082	TENO-A(6)	257×129 × 129	2.0	18.693
Ref.2	–	–	0.082	222	221.6	Spectral	144×119 × 80	–	18.925

Ref.1: Vreman and Kuerten(2014).
Ref.2: Coleman et al.(1995).

Case	Re_τ	Re_{τ_s}	Scheme (Ord.)	Grid	Δx^+_s	Δy^+_s	Δz^+_s
1	180	180.188	Central(4)	129×129 × 129	17.552	0.655	5.850
2	222	221.814	Central(4)	129×129 × 129	21.607	0.807	7.202
2b	222	223.000	Central(4)	257×257 × 257	10.903	0.400	3.634
3	222	222.248	Central(4)	257×129 × 129	10.867	0.808	7.216
4	222	222.614	Central(4)	129×257 × 129	21.685	0.400	7.228
5	222	221.921	Central(4)	129×129 × 257	21.618	0.807	3.617
6	222	222.199	Central(6)	129×129 × 129	21.645	0.808	7.215
7	222	223.737	TENO(6)	129×129 × 129	21.795	0.814	7.265
8	222	223.174	TENO(6)	257×129 × 129	10.912	0.812	7.246
9	222	223.805	TENO(6)	129×257 × 129	21.801	0.402	7.267
10	222	223.920	TENO(6)	129×129 × 257	21.812	0.814	3.649
11	222	226.891	WENO-Z(5)	129×129 × 129	22.102	0.825	7.367
12	222	227.144	WENO-JS(5)	129×129 × 129	22.127	0.826	7.375
13	222	224.337	TENO(5)	129×129 × 129	21.853	0.816	7.284
14	222	223.153	TENO-A(5)	129×129 × 129	21.738	0.812	7.246
15	222	222.807	TENO-A(6)	129×129 × 129	21.704	0.810	7.234
16	222	222.082	TENO-A(6)	257×129 × 129	10.859	0.808	7.211

a finite difference code and a spectral code, and provided a comprehensive discussion and comparison against the literature data. In the present work the channel flow case with $Re_\tau = 180$ is used to evaluate the performance of OpenSBLI as a preliminary validation. This is test case 1 of table 1 and is compared against the spectral results of Vreman and Kuerten[46]. Figure 2 shows a direct comparison between OpenSBLI results obtained with the 4^{th} order central scheme and the spectral results of[46] based on the mean streamwise velocity and the root mean square (rms) of the fluctuations of the velocity components. OpenSBLI is

a compressible solver therefore a friction Mach number of $M_\tau^* = 0.01$ is used to mimic incompressible conditions. Also, to maintain a stable solution the solver requires a smaller time step ($\Delta t = 5 \times 10^{-5}$) compared to incompressible solvers which typically require a time step that ranges from 10^{-4} to 10^{-3} depending on the numerical method and spatial resolution[46]. Figure 2 includes OpenSBLI results for statistics collection duration $T = 500$ and $T = 1000$. It is evident that statistical convergence is obtained even with $T = 500$. Nevertheless, in the present work all results are evaluated at $T = 1000$.

With respect to the mean streamwise velocity a very good agreement is found between OpenSBLI and the spectral DNS of[46]. The mean centreline velocity is calculated to be $\langle u_c \rangle = 18.295$ which is around 0.18% higher than that of the reference data[46]. However, there are slight deviations in the rms of velocity fluctuations, particularly close to the channel centreline, as shown in figure 2. Specifically, the rms of velocity fluctuations at the channel centreline are $u_{rms} = 0.738$, $v_{rms} = 0.588$ and $w_{rms} = 0.575$ which are 7.28%, 3.90% and 6.35% lower than those of the spectral DNS of[46], respectively. Also, the peak of the rms of velocity fluctuations are $u_{rms} = 2.558$, $v_{rms} = 0.841$ and $w_{rms} = 1.084$ which are 3.94%, 0.11% and 0.36% lower than those of the spectral reference data, respectively. These slight differences are mainly attributed to the spatial resolution, particularly in the streamwise direction, which will be discussed again later in this paper.

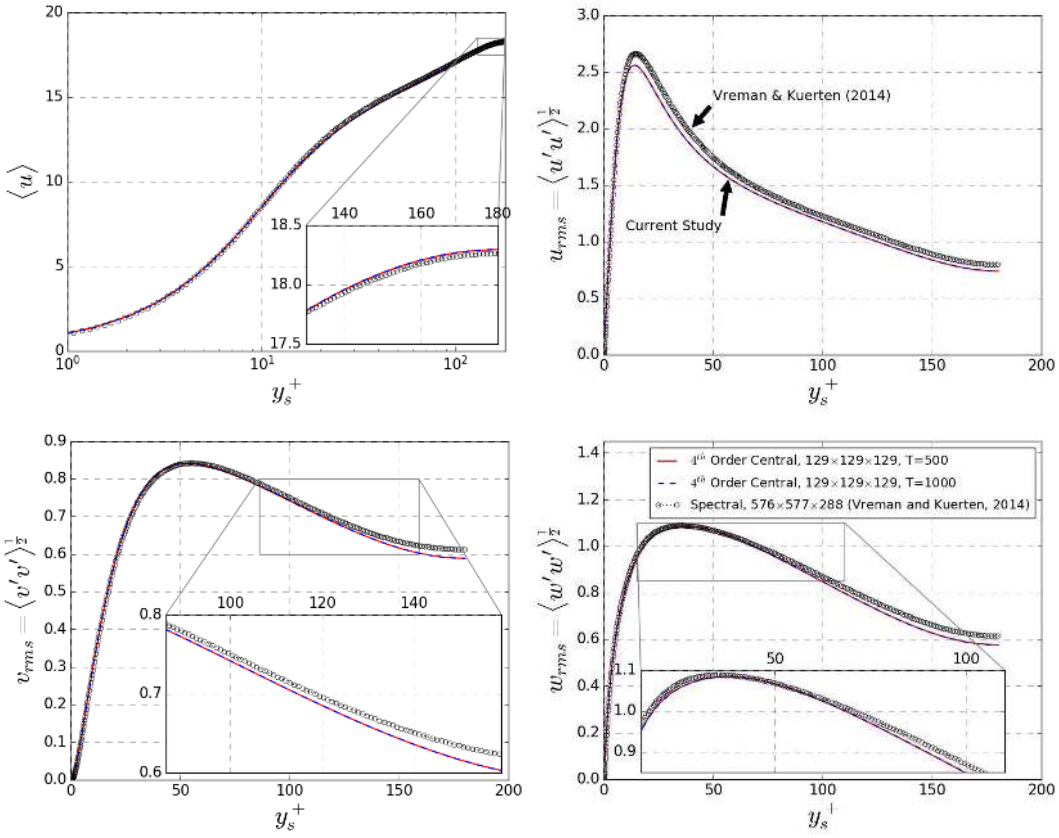

FIGURE 2 Mean streamwise velocity and normal Reynolds stresses for the incompressible case with $Re_\tau = 180$.

4.2 | Supersonic channel flow

4.2.1 | Scheme comparison

Various high-order shock capturing schemes, including central, WENO and TENO schemes, are used to perform DNS of the compressible turbulent channel flow case with $Re_\tau = 222$ and $M_\tau = 0.082$ ($M = 1.5$). Figure 3 shows a comparison based on various mean flow parameters, including the streamwise velocity, Mach number, density and temperature between the present

DNS, using various high-order schemes and a spectral reference DNS conducted by Coleman et al.[47]. Values of the obtained friction Reynolds numbers ($Re^*_{\tau_s}$ and Re_{τ_s}) and the mean streamwise velocity at the channel centreline ($\langle u_c \rangle$) are tabulated in table 1. The central schemes show the closest agreement to the reference data for all mean flow parameters presented in figure 3. Also, the TENO schemes show a much better performance compared to the WENO schemes, with the 6^{th} order TENO-A scheme showing the closest agreement to the reference data along with the central schemes. For instance, the 4^{th} and 6^{th} order central schemes give 0.258% and 0.179% lower mean streamwise velocities at the channel centreline compared to the reference data ($\langle u_c \rangle = 18.925$), respectively. The 6^{th} order TENO scheme and the 6^{th} order TENO-A scheme give a 0.634% higher and 0.147% lower mean streamwise velocity at the channel centreline compared to the reference data, respectively. On the other hand, the 5^{th} order WENO-JS and after that the 5^{th} order WENO-Z exhibit the worst performance in predicting the mean flow quantities shown in figure 3. The latter schemes give 7.98% and 4.97% higher mean streamwise centreline velocities compared to the reference data, respectively.

A direct comparison based on the mean Reynolds stresses between various high-order schemes studied here on the 129×129×129 grid and the reference solution of Coleman et al.[47] is shown in figure 4. Moreover, corresponding peak values of the stresses shown in figure 4 are provided in table 2. A similar trend to what observed for the mean flow parameters is also seen for the Reynolds stresses. Specifically, the central schemes exhibit the closest behaviour to the references data, followed by the 6^{th} order TENO-A scheme. The WENO schemes perform poorly again compared to the other schemes. The central schemes give very close trends to the reference data for the $\langle u'u' \rangle$ and $\langle v'v' \rangle$ stresses. The 6^{th} order TENO-A also exhibits a good performance for these stresses. Comparing against the reference data, it is found that the peak $\langle u'u' \rangle$ stress is 1.69% lower, 0.55% higher, 3.37% higher and 33.57% higher with the 4^{th} order central, 6^{th} order central, 6^{th} order TENO-A and 5^{th} order WENO-JS schemes, respectively.

With respect to the shear stress $\langle u'v' \rangle$ all schemes exhibit a similar behaviour except for the WENO schemes which give noticeably lower peak values. WENO-JS gives 4.25%, 3.26% and 6.31% lower values for the $\langle u'v' \rangle$ stress compared to the 4^{th} order central, the 6^{th} order TENO-A scheme and the spectral reference DNS, respectively. A comparable trend to what is observed here in figures 3 and 4 is also reported by Lusher and Sandham[8]. Particularly, the 6^{th} order TENO-A scheme performed very well in predicting statistical quantities on relatively coarse grids[8].

TABLE 2 Peak mean Reynolds stresses for the current DNS simulations with different high-order schemes on the 129×129×129 grid compared to those of the spectral reference data.

Scheme	$\langle u'u' \rangle$	$\langle v'v' \rangle$	$\langle w'w' \rangle$	-$\langle u'v' \rangle$
4^{th} Order Central	7.312	0.624	1.016	0.682
6^{th} Order Central	7.479	0.626	1.026	0.678
5^{th} Order WENO-Z	9.069	0.506	0.843	0.651
5^{th} Order WENO-JS	9.935	0.482	0.797	0.653
5^{th} Order TENO	8.397	0.557	0.918	0.669
6^{th} Order TENO	7.895	0.587	0.963	0.669
5^{th} Order TENO-A	7.976	0.589	0.965	0.673
6^{th} Order TENO-A	7.689	0.607	0.992	0.675
Spectral (Coleman et al.)	7.438	0.645	1.102	0.697

There are various methods for vortex identification which can be used to visualise vortical structures in turbulent flows[49]. Among them, Q criterion is one of the widely used methods to visualise complex vortical features. Q identifies vortex cores in a three-dimensional flow as connected regions where the vorticity $\boldsymbol{\Omega}$ prevails over the strain rate $\boldsymbol{S}$[49,50,51]. Specifically, based on its definition there exists a vortex core where $Q = \frac{1}{2}(\| \boldsymbol{\Omega} \|^2 - \| \boldsymbol{S} \|^2) > 0$. However, this is only valid for incompressible flows where Q is directly related to the second invariant of the velocity gradient ($II_{\nabla \boldsymbol{u}}$). For compressible flows the divergence of the velocity field is non-zero, hence $II_{\nabla \boldsymbol{u}} \neq Q$. Therefore, as discussed in[50,51], the extension of Q to compressible flows suffers from ambiguity and fails as a correct vortex identification criterion. Recently, Kolář and Šístek[51] suggested a modification to Q which introduces compressibility and kinematic corotational aspects required for vortex identification in compressible flows. This approach is named Q_M and defines as $Q_M = Q + {}^{II_S}/_2$ where II_S is the second invariant of $\boldsymbol{S}$[51].

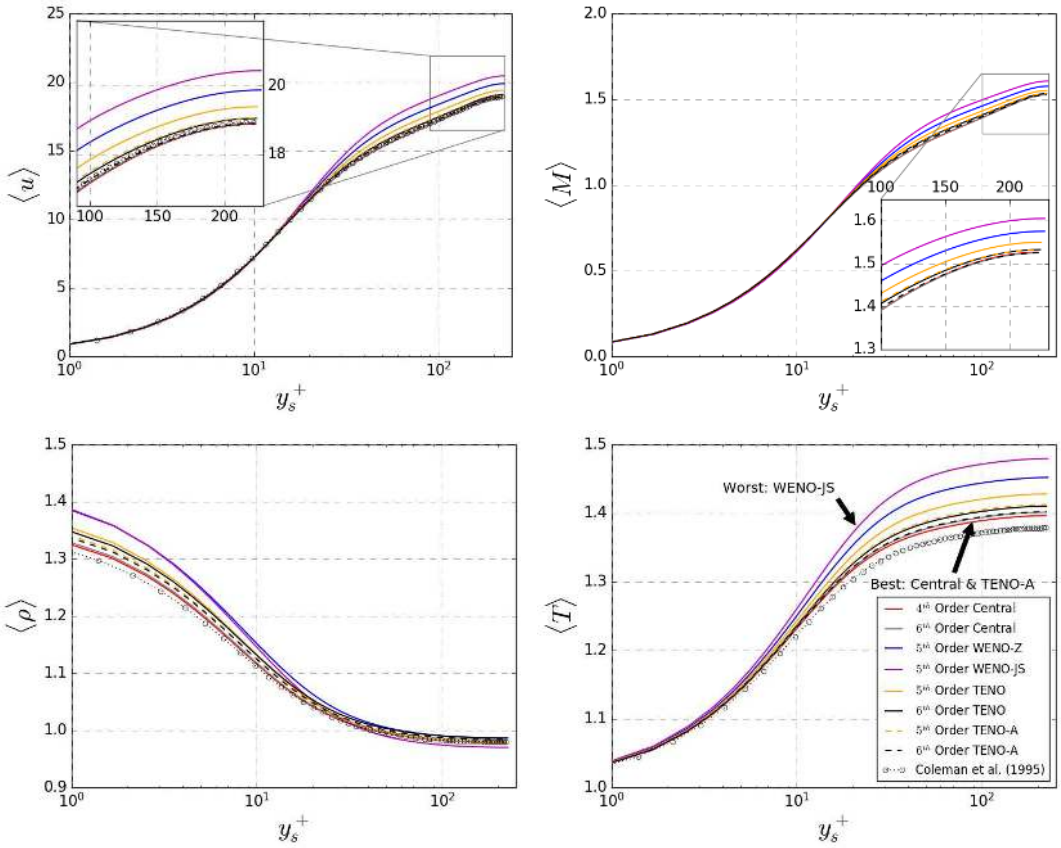

FIGURE 3 Mean streamwise velocity, Mach number, density and temperature for the compressible case with $Re_\tau = 222$.

In the present study Q_M is used to make a qualitative comparison of the accuracy of the aforementioned high-order schemes to predict vortical turbulent structures. Specifically, iso-surfaces of Q_M with an iso-value of $Q_{M_{iso}} = 30$ are visualised for the DNS cases of table 1 with the $129 \times 129 \times 129$ grid resolution as shown in figure 5. It should be noted that figure 5 only shows the iso-surfaces which are located within the lower half of the channel to provide a more clear presentation. Large vortical structures which are mainly elongated in the streamwise direction are seen in the flow field of all schemes studied here. However, the schemes with a higher order of accuracy and/or an inherently lower dissipation capture a higher number of such elongated structures and noticeably more medium and small size structures. Specifically, the non-dissipative central schemes show a dense field with a wide range of vortex sizes. The TENO-A and TENO schemes show slightly less features compared to the central schemes, but still capture a wide range of structures. Nevertheless, the TENO-A schemes seem to better capture the medium and small size vortices compared to their baseline TENO counterparts with the same order of accuracy. On the other hand, the WENO schemes perform poorly by failing to capture a wide range of structures compared to the central and TENO family schemes. In fact, the WENO schemes generally only capture the large elongated vortical structures. The performance shown in figure 5 supports the earlier discussion provided based on figures 3 and 4 for the accuracy of the high-order schemes. The elongated structures are formed when near-wall vortices are stretched by shear forces. The near-wall structures are created when the vortices formed in the viscous layer are ejected into the outer layers. This vortex ejection mechanism can be seen in all snapshots of figure 5 in locations where the vortical structures are almost attached to the wall. A comparable behaviour and sensitivity to the numerical scheme and the discretisation order, to what is shown in figure 5, are reported in[52] for a weakly-compressible TCF with various schemes including WENO. Specifically, with the WENO scheme, 5^{th} order of accuracy was not enough to capture the vortical structures and the flow statistics with an acceptable level of accuracy and only a 9^{th} order WENO scheme exhibited a reasonable performance[52].

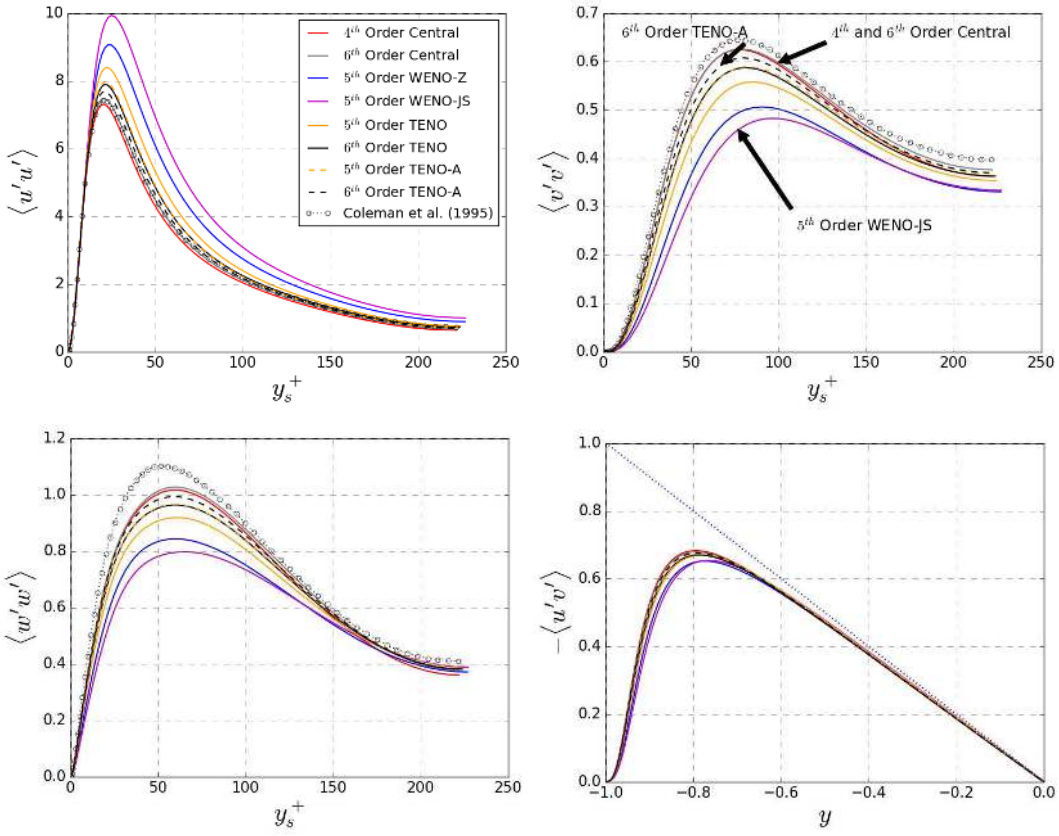

FIGURE 4 Mean Reynolds stresses for the compressible case with $Re_\tau = 222$.

4.2.2 | Computational cost

The computational cost associated with a high-order scheme is of great importance particularly for high fidelity DNS. Table 3 provides the total wall time for 250000 iterations of the compressible TCF DNS case on the $129 \times 129 \times 129$ grid for all the high-order schemes studied here. The wall time is for one NVIDIA Tesla P100 GPU of Imperial College London's High Performance Computing facility.

The central schemes are the most efficient ones in terms of the computational cost. The 4^{th} order central scheme, which has the lowest cost, is selected as the reference to calculate the relative costs provided in table 3. The 6^{th} order central scheme is only 8.2% more expensive than its 4^{th} order counterpart. The high-order central schemes, considering their excellent performance (as shown in figures 3 and 4) and noticeably lower computational costs compared to the other schemes, are the most attractive schemes for DNS of compressible turbulent flows where shockwaves and flow discontinuities do not exist. However, when shock-capturing is required the WENO schemes are the most efficient ones in terms of the computational cost, with 17.2% and 17.8% relative costs for the WENO-JS and WENO-Z schemes, respectively. The WENO-Z scheme is preferred over the WENO-JS since it has only 0.52% higher computational cost but exhibits a much better performance as seen in figures 3 and 4. The 5^{th} order TENO scheme has only around 5% higher relative cost compared to the 5^{th} order WENO-Z scheme but it shows a much better performance and should be considered if an average accuracy and a moderate computational cost are required. The adaptive schemes evaluate the sock sensor and therefore have a relatively higher computational costs compared to their standard counterparts. Nevertheless, the 6^{th} order TENO-A scheme is recommended for when shock capturing is required and the priority is to obtain a more precise solution with respect to the turbulent structures. A similar computational cost trend as discussed here for the WENO and TENO schemes is also reported for a TGV problem using the OpenSBLI framework in [8].

It is worth mentioning that the computational efficiency of WENO/TENO based schemes can be noticeably increased by using a hybrid approach in which a corresponding optimal linear scheme is applied in smooth regions [53,54]. For instance, Fu [54] reported a near 4 times speedup for a hybrid TENO scheme compared to a pure TENO scheme for a 2D Riemann problem. Nevertheless,

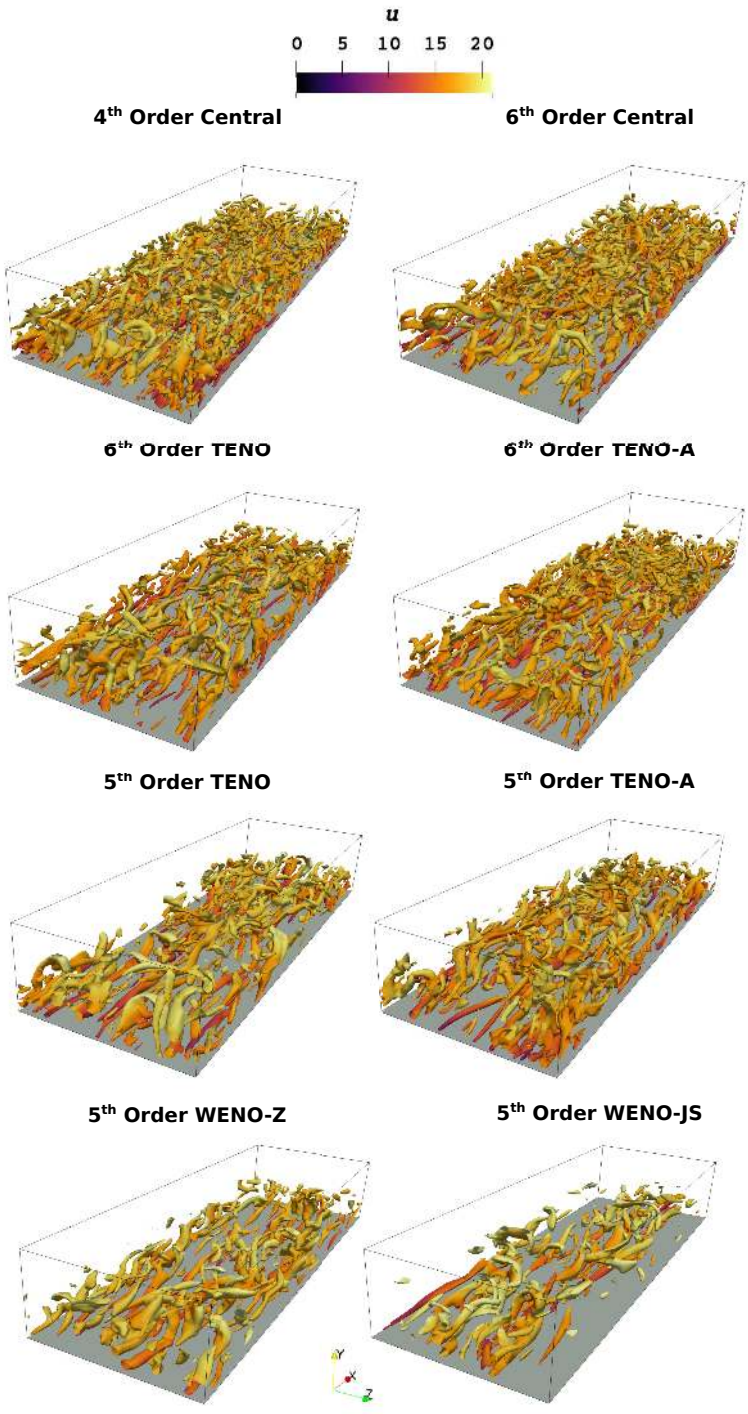

FIGURE 5 Q_M iso-surfaces on the $129 \times 129 \times 129$ grid with an iso-value of $Q_{M_{iso}} = 30$ coloured by the streamwise velocity for different schemes at $t = 50$ (the compressible case with $Re_\tau = 222$). The iso-surfaces are only visualised for the lower half of the channel.

as shown in table 3, the most computationally expensive TENO scheme used here has only around 45% higher cost compared to the baseline central scheme which has significantly fewer operations in comparison to the aforementioned hybrid TENO scheme.

This indicates that obtaining a significant speedup by applying a similar hybrid approach is not plausible here and the TENO scheme used in this study is relatively well optimised (also, further modifications may cause load balancing issues).

TABLE 3 Total wall time for 250000 iterations of the compressible TCF DNS with different high-order schemes on the $129 \times 129 \times 129$ grid using one 16GB NVIDIA Tesla P100 GPU (CUDA 8.0). The relative computational cost is compared against the 4^{th} order central scheme.

Scheme	Total Wall Time [s]	Relative Cost [%]
4^{th} Order Central	10503	0.0
6^{th} Order Central	11365	8.2
5^{th} Order WENO-JS	12310	17.2
5^{th} Order WENO-Z	12375	17.8
5^{th} Order TENO	12987	23.6
5^{th} Order TENO-A	14025	33.5
6^{th} Order TENO	14242	35.6
6^{th} Order TENO-A	15260	45.3

4.2.3 | Grid refinement study

In this section the effect of the spatial resolution is studied by increasing the grid resolution from 129 to 257 in each direction separately for the 4^{th} order central scheme and the 6^{th} order TENO and TENO-A schemes. Also, a central test case on a $257 \times 257 \times 257$ grid is examined. Figures 6 and 7 show the mean streamwise velocity and the mean normal stresses for the aforementioned schemes with different spatial resolutions. Corresponding peak values of the normal stresses are also tabulated in table 4. The mean streamwise velocity is calculated fairly well with the central and TENO schemes as discussed earlier and therefore increasing the grid resolution does not provide a noticeable improvement as seen in figures 6 and 7. On the other hand, with respect to the normal stresses, increasing the resolution in the streamwise direction significantly enhances the performance of all schemes studied here, particularly the TENO schemes.

With the central scheme, increasing the resolution in the streamwise direction noticeably improves the performance for $y_s^+ \geq 80$ where comparable values to those of the spectral reference data are obtained. However, it results in the overprediction of the peak $\langle u'u' \rangle$ stress by 3.17% compared to the reference data. On the other hand, refining the spatial resolution in the y and z directions results in lower peak values of the $\langle u'u' \rangle$ stress by 1.55% and 2.03%, respectively. The central scheme produces similar results on the $257 \times 257 \times 257$ grid to those of the $257 \times 129 \times 129$ grid and no significant improvements are gained by refining the spatial resolution in all directions at once as can be seen in figure 6 and table 4.

With the 6^{th} order TENO and TENO-A schemes, increasing the grid resolution in the streamwise direction has a significant effect on the $\langle u'u' \rangle$ stress and the $\langle v'v' \rangle$ stress. Specifically, it results in around 4.5% and 6.0% improvements in the peak $\langle u'u' \rangle$ and $\langle v'v' \rangle$ stresses, respectively. The $\langle w'w' \rangle$ stress also benefits from increasing the resolution in the streamwise direction, however mainly for $y_s^+ \geq 90$. It can be concluded that a grid resolution of $257 \times 129 \times 129$ with the central and TENO schemes produces satisfactory results for this compressible TCF case within a relatively affordable computational time. The TENO scheme requires 81.5% higher total wall time (for 250000 iterations) on the $257 \times 129 \times 129$ grid compared to the $129 \times 129 \times 129$ grid.

4.3 | Implicit and explicit LES

The main concept of an implicit LES approach is to use the numerical dissipation, arising from discretisation schemes (such as TENO), as a kind of turbulent viscosity comparable to that of an explicit SGS LES model. In this section, we evaluate the possibility of using the central, TENO and TENO-A schemes of OpenSBLI to perform ILES of compressible turbulent channel flows. Also, a direct comparison is conducted between the ILES approach and the WALE LES model which is implemented in OpenSBLI in the present work.

The compressible turbulent channel flow test case with $Re_\tau = 222$ and $M_\tau = 0.082$ is modelled on relatively coarser grids compared to those used for the DNS studies discussed earlier in this paper. specifically, various combinations of grid resolutions

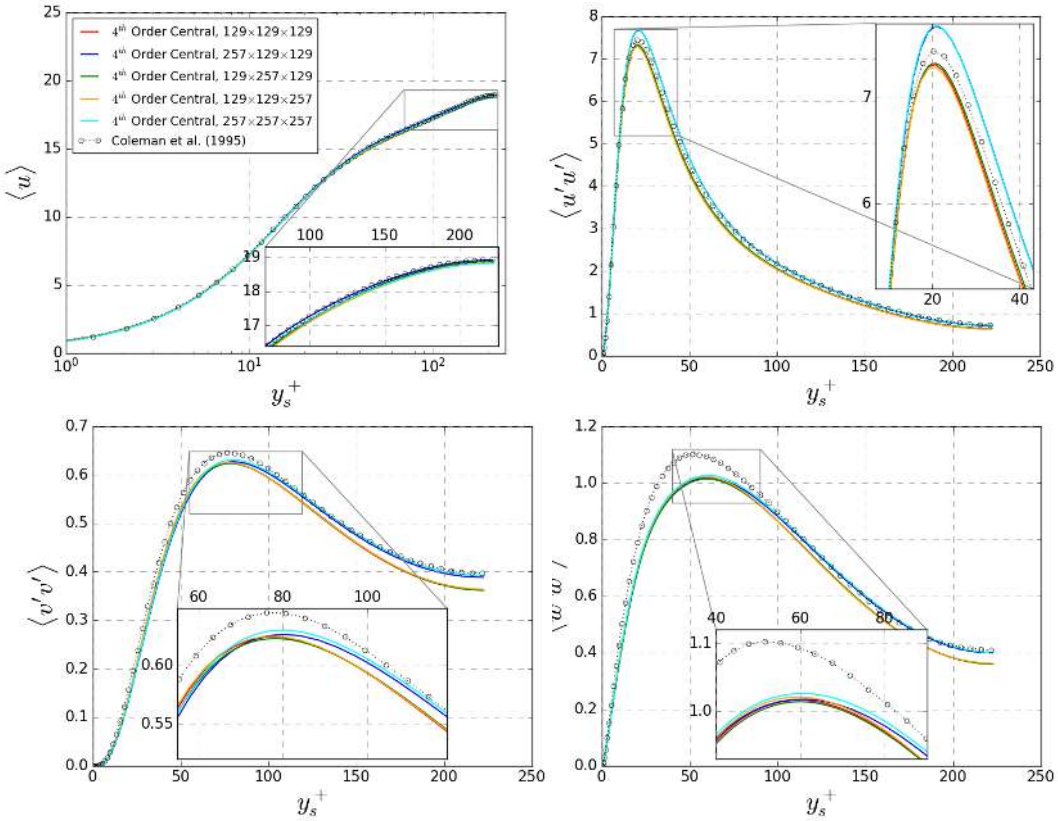

FIGURE 6 Mean streamwise velocity and Reynolds stresses for the compressible case simulated with the 4^{th} order central scheme on various spatial resolutions.

TABLE 4 Peak mean normal Reynolds stresses for different schemes and grid resolutions studied compared to the spectral reference DNS.

Scheme	Grid	$\langle u'u' \rangle$	$\langle v'v' \rangle$	$\langle w'w' \rangle$
4^{th} Order Central	129×129 × 129	7.312	0.624	1.016
4^{th} Order Central	257×129 × 129	7.674	0.626	1.017
4^{th} Order Central	129×257 × 129	7.322	0.623	1.013
4^{th} Order Central	129×129 × 257	7.287	0.625	1.020
4^{th} Order Central	257×257 × 257	7.676	0.630	1.026
6^{th} Order TENO	129×129 × 129	7.895	0.587	0.963
6^{th} Order TENO	257×129 × 129	7.590	0.620	1.01
6^{th} Order TENO	129×257 × 129	7.960	0.591	0.969
6^{th} Order TENO	129×129 × 257	7.813	0.587	0.965
6^{th} Order TENO-A	257×129 × 129	7.563	0.625	1.022
Spectral (Coleman et al.)	144×119 × 80	7.438	0.645	1.102

including 32×129×32 and 64×64×64, high-order schemes and the WALE SGS model are used as presented in table 5. Figures 8 and 9 show direct comparisons based on the mean streamwise velocity and the normal Reynolds stresses of the test cases presented in table 5. It should be noted that with explicit LES modelling some of the turbulent energy is held in the SGS model. Therefore, when making comparison against DNS, it might be more appropriate to also filter the DNS solution and compare the

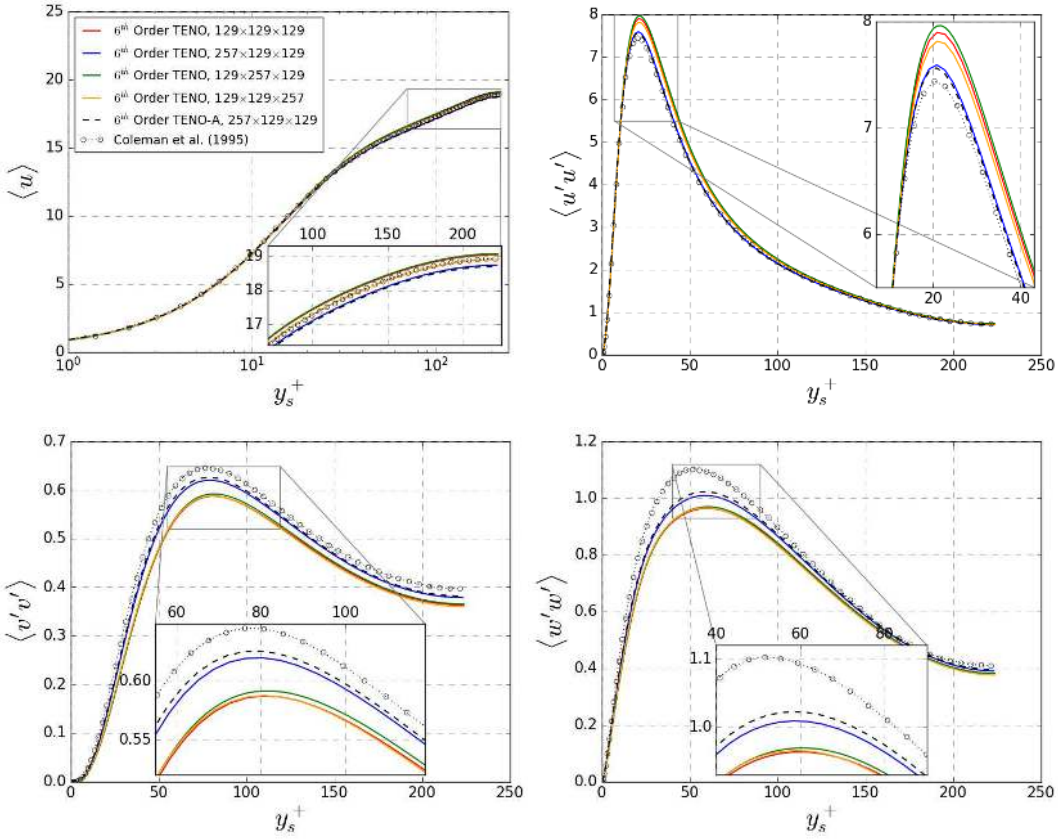

FIGURE 7 Mean streamwise velocity and Reynolds stresses for the compressible case simulated with 6^{th} order TENO and TENO-A schemes on various spatial resolutions.

respective rms fluctuations. However, since in this study ILES modelling is also investigated and compared against DNS and WALE, such filtering is avoided.

The $32 \times 129 \times 32$ grid resolution is used to decouple the effect of the wall y^+ and as given in table 5 the test cases with this resolution have relatively similar Δy_s^+ values to that of the DNS case with $129 \times 129 \times 129$. From figure 8 it is evident that, the WALE model improves the performance of the 4^{th} order central scheme to predict the mean streamwise velocity. However, the central scheme with the WALE model overpredicts the peak $\langle u'u' \rangle$ stress and underpredicts the peak of the other two normal stresses in comparison to when it is used without the SGS model. This is a well-known behaviour and has been reported in the literature[55]. Although the TENO-A scheme improves the prediction of the mean streamiwse velocity as shown in figure 8, it does not show a satisfactory performance in predicting the normal Reynolds stresses on the $32 \times 129 \times 32$ grid resolution. Moreover, from figure 8 it is clear that by reducing C_T of the TENO scheme, from 10^{-7} to 10^{-9}, its ability to predict the mean statistical parameters noticeably improves. In fact, by reducing C_T the numerical dissipation of the scheme reduces. However, this results in a reduced ability to produce a non-spurious stable solution at the location of shockwaves and flow discontinuities.

Similarly to the $32 \times 129 \times 32$ grid resolution, the combination of the WALE model and the central scheme also improves the performance of the code to predict the mean streamwise velocity on the $64 \times 64 \times 64$ resolution as shown in figure 9. A similar trend also exists for the normal stresses as shown in figures 8 and 9. However, since the central scheme without the WALE model underpredicts the $\langle u'u' \rangle$ stress on the $64 \times 64 \times 64$ grid, adding the WALE model results in a very close prediction of $\langle u'u' \rangle$ to that of the reference DNS as shown in figure 9. Comparing against the central scheme with the WALE model, it is evident that the TENO-A scheme exhibits a similar trend for the grid resolutions studied here. From figures 8 and 9 it can be concluded that the combination of the TENO-A scheme and the WALE model is not beneficial and should be avoided. However, the results show that the TENO-A scheme alone may be used as an ILES model for compressible TCFs. From table 5 it is evident that with

the $64 \times 64 \times 64$ resolution, increasing the stretching factor f_s in equation 12 from 1.7 to 1.9 reduces Δy_s^+ by around 24.5%. However this improvement in the wall y^+ value does not seem to noticeably improve the performance as seen in figure 9.

TABLE 5 TCF implicit and explicit LES test cases.

Case	Scheme (Ord.)	Turb.	Grid	f_s	C_T	$Re^*_{\tau_s}$	$Re_{\tau s}$	Δy_s^+	$\langle u_c \rangle$
2	Central(4)	DNS	129×129 × 129	1.7	–	189.336	221.814	0.807	18.876
17	Central(4)	ILES	32×129 × 32	1.7	–	189.210	216.652	0.788	18.042
18	Central(4)	WALE	32×129 × 32	1.7	–	188.339	217.463	0.791	18.654
19	Central(4)	ILES	64×64 × 64	1.7	–	185.335	216.503	1.642	18.098
20	Central(4)	WALE	64×64 × 64	1.7	–	184.641	217.824	1.652	18.602
7	TENO(6)	DNS	129×129 × 129	1.7	10^{-7}	190.136	223.737	0.814	19.045
21	TENO(6)	ILES	32×129 × 32	1.7	10^{-7}	189.156	234.029	0.851	22.516
22	TENO(6)	ILES	32×129 × 32	1.7	10^{-9}	189.306	226.856	0.825	20.408
15	TENO-A(6)	DNS	129×129 × 129	1.7	–	189.837	222.807	0.810	18.897
23	TENO-A(6)	ILES	32×129 × 32	1.7	–	189.445	222.448	0.809	19.076
24	TENO-A(6)	WALE	32×129 × 32	1.7	–	189.133	223.515	0.813	19.538
25	TENO-A(6)	ILES	64×64 × 64	1.7	–	185.574	221.110	1.677	19.024
26	TENO-A(6)	ILES	64×64 × 64	1.9	–	186.734	221.951	1.270	19.017
27	TENO-A(6)	WALE	64×64 × 64	1.7	–	185.367	222.316	1.686	19.449

5 | CONCLUSIONS

The performance of a selection of low-dissipative high-order shock capturing schemes to model compressible turbulent flows was quantified and investigated. The focus was on the capability of those schemes to resolve turbulent structures. Therefore, a channel flow configuration was used to decouple the effect of flow discontinuities and turbulence. Specifically, DNS studies were conducted on subsonic ($Re_\tau = 180$) and supersonic ($M = 1.5$ and $Re_\tau = 222$) turbulent channel flows using OpenSBLI, a Python-based automatic source code generation and parallel computing framework for finite difference discretisation. The schemes studied here were 4^{th} and 6^{th} order central, 5^{th} order WENO-Z and WENO-JS, and 5^{th} and 6^{th} order TENO and adaptive TENO (TENO-A) schemes. Also, a comprehensive study was conducted to evaluate the effect of the spatial resolution on the performance of the central and TENO schemes. Moreover, the accuracy of the TENO family schemes as ILES models was evaluated against DNS and the WALE SGS model.

Significant improvements were achieved using the TENO scheme, and particularly the TENO-A scheme, over the WENO schemes with respect to the mean and fluctuating flow quantities in DNS of the compressible TCF. Also, the TENO schemes captured the three-dimensional vortical structures very close to the non-dissipative central schemes and much better than the WENO schemes that failed to resolve a wide range of structures particularly the medium and small size vortices.

It was observed that using the WALE model in conjunction with the WENO and TENO schemes resulted in undesirable additional dissipation and should be avoided. However, the TENO family schemes were found to be appropriate for ILES. For instance, reducing the value of the C_T constant in the TENO scheme, from 10^{-7} to 10^{-9}, improved its performance as an ILES model. However, it was still more dissipative than the TENO-A scheme on a similar coarse grid. A further reduction in the C_T value would be required to be able to appropriately use the TENO scheme as an ILES model for the compressible TCF case. On the other hand, the TENO-A scheme exhibited a reasonable performance, particularly for the mean streamwise velocity ($\langle u \rangle$) and the $\langle u'u' \rangle$ normal stress. This scheme showed the best potential to be applied as an ILES model, with only modest increases in computational costs, for shock-containing turbulent flows.

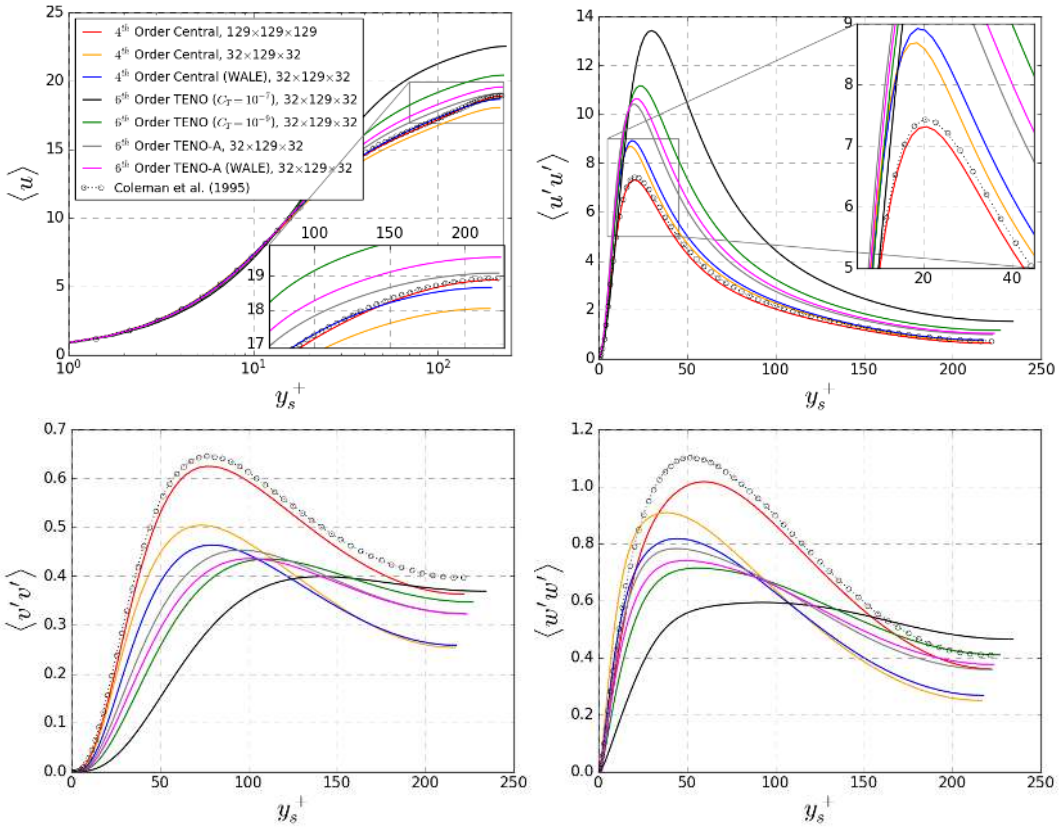

FIGURE 8 Mean streamwise velocity and normal Reynolds stresses for the WALE and ILES TCF cases on the $32 \times 129 \times 32$ grid.

ACKNOWLEDGMENTS

Dr Arash Hamzehloo is funded by the UK Turbulence Consortium (UKTC) under the EPSRC grant EP/R029326/1. He also received a Short Research Visit (SRV) funding from the UK Fluids Network (EP/N032861/1) over the course of this work. Dr David J Lusher was funded by an EPSRC Centre for Doctoral Training grant (EP/L015382/1). Dr Arash Hamzehloo acknowledges the use of Imperial College London's High Performance Computing Facility and associated support services to conduct the simulations presented in this paper. Dr Arash Hamzehloo also acknowledges the use of the Cambridge Tier-2 system operated by the University of Cambridge Research Computing Service under an EPSRC Tier-2 capital grant (EP/P020259/1) to perform part of simulations reported here. The OpenSBLI code is available at https://opensbli.github.io. Data from this study will be made available from the UKTC and the Turbulence Simulation Group repositories.

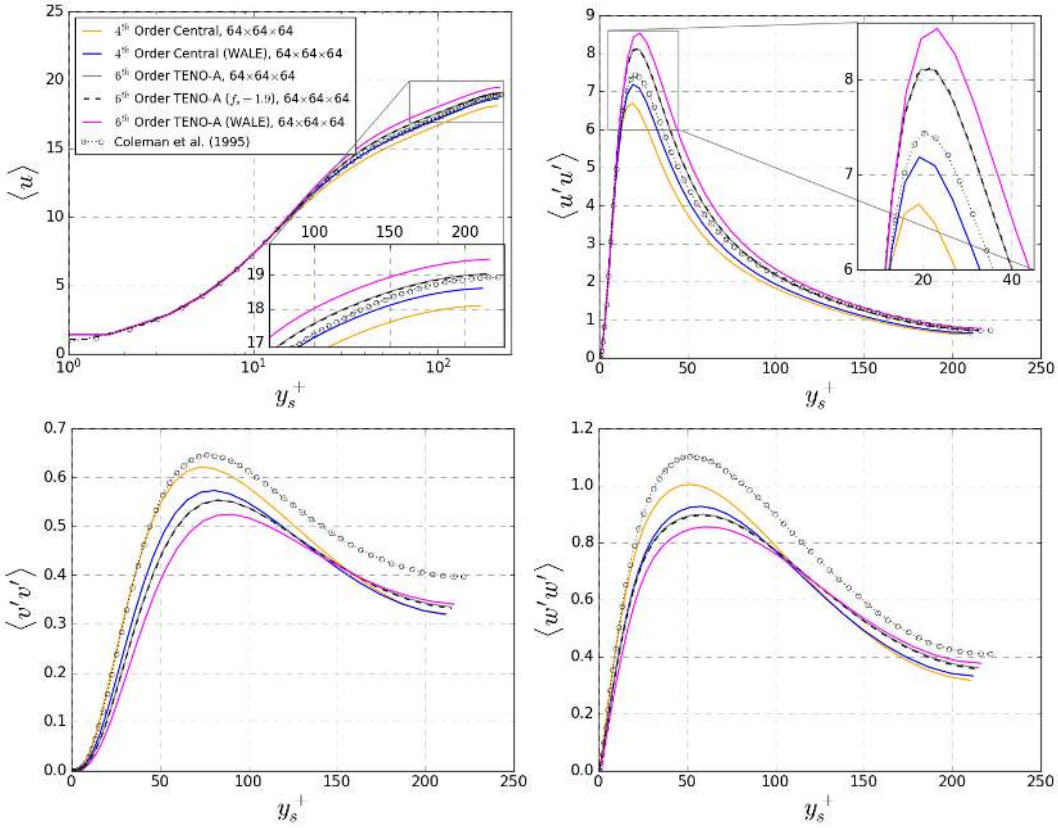

FIGURE 9 Mean streamwise velocity and normal Reynolds stresses for the WALE and ILES TCF cases on the 64×64×64 grid.

References

1. Urzay J. Supersonic combustion in air-breathing propulsion systems for hypersonic flight. *Annual Review of Fluid Mechanics* 2018; 50: 593–627.

2. Braun N, Pullin D, Meiron D. Large eddy simulation investigation of the canonical shock–turbulence interaction. *Journal of Fluid Mechanics* 2019; 858: 500–535.

3. Chen CH, Donzis DA. Shock–turbulence interactions at high turbulence intensities. *Journal of Fluid Mechanics* 2019; 870: 813–847.

4. Farag G, Boivin P, Sagaut P. Interaction of two-dimensional spots with a heat releasing/absorbing shock wave: linear interaction approximation results. *Journal of Fluid Mechanics* 2019; 871: 865–895.

5. Hortensius R, Dutton JC, Elliott GS. Near field of an axisymmetric underexpanded jet and an adjacent parallel surface. *AIAA Journal* 2017: 2489–2502.

6. Jiang GS, Shu CW. Efficient implementation of weighted ENO schemes. *Journal of computational physics* 1996; 126(1): 202–228.

7. Shu CW. Essentially non-oscillatory and weighted essentially non-oscillatory schemes for hyperbolic conservation laws. In: Springer. 1998 (pp. 325–432).

8. Lusher DJ, Sandham N. Assessment of low-dissipative shock-capturing schemes for transitional and turbulent shock interactions. In: ; 2019: 3208.

9. Mossi M, Sagaut P. Numerical investigation of fully developed channel flow using shock-capturing schemes. *Computers & fluids* 2003; 32(2): 249–274.

10. Gerolymos G, Sénéchal D, Vallet I. Performance of very-high-order upwind schemes for DNS of compressible wall-turbulence. *International Journal for Numerical Methods in Fluids* 2010; 63(7): 769–810.

11. Henrick AK, Aslam TD, Powers JM. Mapped weighted essentially non-oscillatory schemes: achieving optimal order near critical points. *Journal of Computational Physics* 2005; 207(2): 542–567.

12. Martín MP, Taylor EM, Wu M, Weirs VG. A bandwidth-optimized WENO scheme for the effective direct numerical simulation of compressible turbulence. *Journal of Computational Physics* 2006; 220(1): 270–289.

13. Taieb D, Ribert G. Direct numerical simulation and large-eddy simulation of supersonic channel flow. *Journal of Propulsion and Power* 2013; 29(5): 1064–1075.

14. Ribert G, Taieb D, Yang V. Large-eddy simulation of a supercritical channel flow using a shock capturing numerical scheme. *Computers & Fluids* 2015; 117: 103–113.

15. Matsuyama S. Performance of all-speed AUSM-family schemes for DNS of low Mach number turbulent channel flow. *Computers & Fluids* 2014; 91: 130–143.

16. Borges R, Carmona M, Costa B, Don WS. An improved weighted essentially non-oscillatory scheme for hyperbolic conservation laws. *Journal of Computational Physics* 2008; 227(6): 3191–3211.

17. Houim RW, Kuo KK. A low-dissipation and time-accurate method for compressible multi-component flow with variable specific heat ratios. *Journal of Computational Physics* 2011; 230(23): 8527–8553.

18. Taylor EM, Wu M, Martín MP. Optimization of nonlinear error for weighted essentially non-oscillatory methods in direct numerical simulations of compressible turbulence. *Journal of Computational Physics* 2007; 223(1): 384–397.

19. Lagha M, Kim J, Eldredge J, Zhong X. A numerical study of compressible turbulent boundary layers. *Physics of fluids* 2011; 23(1): 015106.

20. Duan L, Choudhari MM, Wu M. Numerical study of acoustic radiation due to a supersonic turbulent boundary layer. *Journal of Fluid Mechanics* 2014; 746: 165–192.

21. Johnsen E, Larsson J, Bhagatwala AV, et al. Assessment of high-resolution methods for numerical simulations of compressible turbulence with shock waves. *Journal of Computational Physics* 2010; 229(4): 1213–1237.

22. Brehm C, Barad MF, Housman JA, Kiris CC. A comparison of higher-order finite-difference shock capturing schemes. *Computers & Fluids* 2015; 122: 184–208.

23. Hu X, Wang Q, Adams NA. An adaptive central-upwind weighted essentially non-oscillatory scheme. *Journal of Computational Physics* 2010; 229(23): 8952–8965.

24. Ghosh D, Baeder JD. Compact reconstruction schemes with weighted ENO limiting for hyperbolic conservation laws. *SIAM Journal on Scientific Computing* 2012; 34(3): A1678–A1706.

25. Karami S, Stegeman PC, Ooi A, Soria J. High-order accurate large-eddy simulations of compressible viscous flow in cylindrical coordinates. *Computers & Fluids* 2019; 191: 104241.

26. Zhao GY, Sun MB, Pirozzoli S. On shock sensors for hybrid compact/WENO schemes. *Computers & Fluids* 2020: 104439.

27. Hoffmann N, Delorme YT, Frankel SH. High-Order Large Eddy Simulations of High-Speed Boundary Layer Transition. In: ; 2020: 0033.

28. Kotov D, Yee HC, Wray AA, Sjögreen B, Kritsuk AG. Numerical dissipation control in high order shock-capturing schemes for LES of low speed flows. *Journal of Computational Physics* 2016; 307: 189–202.

29. Sjögreen B, Yee H. High order entropy conservative central schemes for wide ranges of compressible gas dynamics and MHD flows. *Journal of Computational Physics* 2018; 364: 153–185.

30. Yee H, Sjögreen B. Recent developments in accuracy and stability improvement of nonlinear filter methods for DNS and LES of compressible flows. *Computers & Fluids* 2018; 169: 331–348.

31. Sjögreen B, Yee H, Wray A. Skew-symmetric splitting of high-order central schemes with nonlinear filters for computational aeroacoustics turbulence with shocks. *Shock Waves* 2019; 29(8): 1117–1132.

32. Fu L, Hu XY, Adams NA. A family of high-order targeted ENO schemes for compressible-fluid simulations. *Journal of Computational Physics* 2016; 305: 333–359.

33. Fu L, Hu XY, Adams NA. Targeted ENO schemes with tailored resolution property for hyperbolic conservation laws. *Journal of Computational Physics* 2017; 349: 97–121.

34. Fu L, Hu XY, Adams NA. A new class of adaptive high-order targeted ENO schemes for hyperbolic conservation laws. *Journal of Computational Physics* 2018; 374: 724–751.

35. Fu L, Hu XY, Adams NA. Improved Five-and Six-Point Targeted Essentially Nonoscillatory Schemes with Adaptive Dissipation. *AIAA Journal* 2018; 57(3): 1143–1158.

36. Sandham ND, Li Q, Yee HC. Entropy splitting for high-order numerical simulation of compressible turbulence. *Journal of Computational Physics* 2002; 178(2): 307–322.

37. Jacobs CT, Jammy SP, Sandham ND. OpenSBLI: A framework for the automated derivation and parallel execution of finite difference solvers on a range of computer architectures. *Journal of Computational Science* 2017; 18: 12–23.

38. Lusher DJ, Jammy SP, Sandham ND. Shock-wave/boundary-layer interactions in the automatic source-code generation framework OpenSBLI. *Computers & Fluids* 2018; 173: 17–21.

39. Ducros F, Ferrand V, Nicoud F, et al. Large-eddy simulation of the shock/turbulence interaction. *Journal of Computational Physics* 1999; 152(2): 517–549.

40. Carpenter MH, Nordström J, Gottlieb D. A stable and conservative interface treatment of arbitrary spatial accuracy. *Journal of Computational Physics* 1999; 148(2): 341–365.

41. Williamson J. Low-storage runge-kutta schemes. *Journal of Computational Physics* 1980; 35(1): 48–56.

42. Nicoud F, Ducros F. Subgrid-scale stress modelling based on the square of the velocity gradient tensor. *Flow, turbulence and Combustion* 1999; 62(3): 183–200.

43. Reguly IZ, Mudalige GR, Giles MB, Curran D, McIntosh-Smith S. The OPS domain specific abstraction for multi-block structured grid computations. In: IEEE. ; 2014: 58–67.

44. Mudalige G, Reguly I, Jammy S, Jacobs C, Giles M, Sandham N. Large-scale performance of a DSL-based multi-block structured-mesh application for Direct Numerical Simulation. *Journal of Parallel and Distributed Computing* 2019; 131: 130–146.

45. Laizet S, Lamballais E. High-order compact schemes for incompressible flows: A simple and efficient method with quasi-spectral accuracy. *Journal of Computational Physics* 2009; 228(16): 5989–6015.

46. Vreman A, Kuerten JG. Comparison of direct numerical simulation databases of turbulent channel flow at Re τ= 180. *Physics of Fluids* 2014; 26(1): 015102.

47. Coleman GN, Kim J, Moser R. A numerical study of turbulent supersonic isothermal-wall channel flow. *Journal of Fluid Mechanics* 1995; 305: 159–183.

48. Kim J, Moin P, Moser R. Turbulence statistics in fully developed channel flow at low Reynolds number. *Journal of fluid mechanics* 1987; 177: 133–166.

49. Haller G. An objective definition of a vortex. *Journal of fluid mechanics* 2005; 525: 1–26.

50. Kolár V. Compressibility effect in vortex identification. *AIAA journal* 2009; 47(2): 473–475.

51. Kolář V, Šístek J. Corotational and compressibility aspects leading to a modification of the vortex-identification Q-criterion. *AIAA Journal* 2015; 53(8): 2406–2410.

52. Kokkinakis I, Drikakis D. Implicit large eddy simulation of weakly-compressible turbulent channel flow. *Computer Methods in Applied Mechanics and Engineering* 2015; 287: 229–261.

53. Hu X, Wang B, Adams NA. An efficient low-dissipation hybrid weighted essentially non-oscillatory scheme. *Journal of Computational Physics* 2015; 301: 415–424.

54. Fu L. A Hybrid Method with TENO Based Discontinuity Indicator for Hyperbolic Conservation Laws. *Communications in Computational Physics* 2019; 26(4): 973–1007.

55. Hickel S, Adams N. On implicit subgrid-scale modeling in wall-bounded flows. *Physics of Fluids* 2007; 19(10): 105106.

56. Kovasznay LS. Turbulence in supersonic flow. *Journal of the Aeronautical Sciences* 1953; 20(10): 657–674.

57. Sagaut P, Cambon C. *Homogeneous turbulence dynamics*. 10. Springer . 2008.

58. Laizet S, Li N. Incompact3d: A powerful tool to tackle turbulence problems with up to O (105) computational cores. *International Journal for Numerical Methods in Fluids* 2011; 67(11): 1735–1757.

59. Dairay T, Lamballais E, Laizet S, Vassilicos JC. Numerical dissipation vs. subgrid-scale modelling for large eddy simulation. *Journal of Computational Physics* 2017; 337: 252–274.

60. Ghosal S. An analysis of numerical errors in large-eddy simulations of turbulence. *Journal of Computational Physics* 1996; 125(1): 187–206.